The electrochemical reduction of dioxygen and hydrogen peroxide by molecular copper catalysts

Langerman, M.

Chapter 5

On the scaling relation between the reduction potential of copper catalysts and the turnover frequency for the oxygen and hydrogen peroxide reduction reactions

Structural changes to the coordination geometry of copper complexes can result in significant changes in their electronic structures, which can have a remarkable impact on the catalytic rates, selectivity, and the overpotential of electrocatalytic reactions. We have investigated the effect of varying the length of the alkyl spacer of one of the pyridine rings in the tris(2-pyridylmethyl)amine (tmpa) ligand on the redox potential of the corresponding pyridylalkylamine copper complexes, and the resulting changes in their catalytic activity for the oxygen reduction reaction in neutral aqueous solution. We confirmed the strong influence of the coordination geometry on the $E_{1/2}$ of the complex, with a more constrained Cu^{I} coordination geometry resulting in the largest positive shift of the redox couple. Likewise, the catalytic onset for the oxygen reduction was equally shifted to a higher potential, resulting in a reduction of the overpotential. All synthesized complexes were shown to catalyse the hydrogen peroxide reduction reaction. A clear linear relationship was established between the maximum rate constants of the reduction of O_2 and H_2O_2, as determined by foot-of-the-wave analysis, and the $E_{1/2}$ of the catalyst, where the catalytic rates decrease as the onset potential increases. Thus, while trade-off between rates and efficiencies remain, significant decreases of the overpotential by 300 mV were achieved by modifying the primary coordination environment of pyridylalkylamine copper complexes.

To be submitted as a full article; M. Langerman, H. van de Vijver, M. A. Siegler, and D. G. H. Hetterscheid, *manuscript in preparation.*

5.1. Introduction

The electrochemical oxygen reduction reaction (ORR) can either result in the four-electron reaction product (H_2O), or the two-electron reaction product (H_2O_2), both involving different standard equilibrium potentials for the respective reactions involved, as shown in Scheme 5.1. Additionally, the four-electron pathway may proceed via H_2O_2 as an intermediate as a result of two consecutive $2H^+/2e^-$ reaction steps. Both the four-electron reduction of dioxygen (O_2) to water and two-electron reduction to H_2O_2 are important reactions, in relation to their application in fuel cell technology, and the use of H_2O_2 as a powerful oxidant and potential energy carrier.[1-7]

$$O_2 + 4H^+ + 4e^- \rightleftharpoons 2H_2O \qquad E^0 = 1.23\ V\ vs.\ RHE$$
$$O_2 + 2H^+ + 2e^- \rightleftharpoons H_2O_2 \qquad E^0 = 0.695\ V\ vs.\ RHE$$
$$H_2O_2 + 2H^+ + 2e^- \rightleftharpoons H_2O \qquad E^0 = 1.78\ V\ vs.\ RHE$$

Scheme 5.1. Standard electrode potentials of the different catalytic reactions involved in the ORR.

As described in Chapter 2, the tetradentate copper complex $[Cu(tmpa)(L)]^{2+}$ (Cu-tmpa) (tmpa = tris(2-pyridylmethyl)amine), L = solvent) has very high reaction rates for the electrochemical ORR.[8] It was shown that the stepwise 4-electron reduction took place, with H_2O_2 observed as a detectable intermediate. Both the partial reduction of O_2 to water (Chapter 2) and the reduction of H_2O_2 (Chapter 3) catalysed by Cu-tmpa demonstrated high catalytic rate constants, with only a small difference in onset potential between the 2-electron ORR and the hydrogen peroxide reduction reaction (HPRR), resulting in only a small potential window where H_2O_2 is the primary product during catalysis. Additionally, the fast catalytic rates for both reactions come at the cost of a significant overpotential. In order to reduce the overpotential and steer the selectivity towards either the full 4-electron or 2-electron reduction of dioxygen, a better fundamental understanding is necessary between the (electronic) structure of the copper catalyst and the catalytic activity for the ORR and HPRR.

The effect of ligand denticity and flexibility on the geometry and electronic structure of copper complexes has been a subject of intense study.[9-17] A significant library of different ligand modifications have been investigated for copper complexes based on the tetradentate pyridine ligand scaffold of Cu-tmpa.[18-20] Interestingly, a larger positive shift of the $Cu^{II/I}$ redox potential (versus Cu-tmpa) is observed for copper complexes with modifications in the length of the alkyl spacer between the central tertiary amine and the pyridine moieties than by adding electron withdrawing or donating functionalities on the pyridine moieties. For the latter, the largest shift of the $Cu^{II/I}$ redox potential was observed for a complex where an -NHR (R = pivaloyl) group

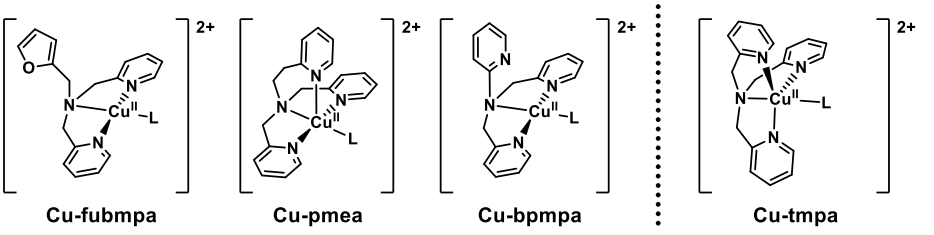

Scheme 5.2. Overview of the structures of the three different copper(II) complexes investigated in this work, in addition to Cu-tmpa.

was substituted on the ortho position of a single pyridine group.[20] The resulting +200 mV shift is significantly less than the shift for some of the complexes with modified alkyl spacer lengths.

We set out to investigate how changes to the tmpa ligand scaffold would affect the catalytic activity of copper complexes for the ORR and HPRR. Desirable changes to the catalytic performance would be a more positive onset potential for the ORR or an increased selectivity for the production of H_2O_2, thereby eliminating or significantly reducing the ability of the catalyst to reduce H_2O_2. Alternatively, increased rates of HPRR versus the ORR could result in a clean 4-electron reduction of oxygen, where no significant amounts of H_2O_2 are produced. Therefore, we investigated three different mononuclear copper complexes, shown in Scheme 5.2. In two of these, $[Cu(pmea)(L)]^{2+}$ (Cu-pmea; pmea = bis[(2-pyridyl)methyl]-2-(2-pyridyl)ethylamine) and $[Cu(bpmpa)(L)]^{2+}$ (Cu-bpmpa; bpmpa = bis[(2-pyridyl)methyl]-2-pyridylamine), the distance between the central tertiary amine and one of the pyridine arms was varied by changing methylene to an ethylene spacer (Cu-pmea) or removing it altogether, resulting in an aminopyridine moiety (Cu-bpmpa). A crystal structure of $[Cu(bpmpa)(Cl)]ClO_4$ shows that the pyridine N of the aminopyridine does not coordinate to the copper centre but is rotated away from the copper centre.[12] The final novel complex, $[Cu(fubmpa)(H_2O)(OTf)_2]$ (Cu-fubmpa; fubmpa = *N*-(furan-2-ylmethyl)-*N*-[bis(2-pyridyl)methyl]amine) was designed as an analogue of the copper complex $[Cu(bmpa)(L)]^{2+}$ (bmpa = bis(2-pyridylmethyl)amine),[21] by introduction of the non-coordinating furanyl moiety while maintaining the nature of the central tertiary amine. Here we show that these ligand-induced changes in the geometry and electronic structure of the copper complexes have a significant impact on the observed catalytic reactivity versus the ORR and HPRR.

5.2. Results and Discussion

5.2.1. Synthesis

The polypyridyl ligands bis[(2-pyridyl)methyl]-2-(2-pyridyl)ethylamine (pmea) and bis[(2-pyridyl)methyl]-2-pyridylamine (bpmpa) have been previously reported and were synthesized in a one-step reaction via reductive amination and nucleophilic substitution (S_N2), respectively.[12] The novel ligand *N*-(furan-2-ylmethyl)-*N*-[bis(2-pyridyl)methyl]amine (fubmpa) was synthesized from the commercially available furan-2-ylmethanamine and 2-pyridinecarboxaldehyde via a reductive amination in a one-step reaction. Following purification by column chromatography, fubmpa was characterized by ^{1}H NMR, ^{13}C NMR and electrospray ionization mass spectrometry (ESI MS). The copper complexes [Cu(pmea)(CH_3CN)](OTf)$_2$ and [Cu(bpmpa)(CH_3CN)](OTf)$_2$ were synthesized by mixing the respective ligand with Cu(OTf)$_2$ in a 1:1 ratio in dry CH_3CN under inert atmosphere, and characterization was performed by ESI MS and elemental analysis (see section 5.4.2). The novel copper complex [Cu(fubmpa)(H_2O)(OTf)$_2$] was synthesized by mixing fubmpa with Cu(OTf)$_2$ in a 1:1 ratio in CH_3CN. The resulting complex was purified by crystallizing the complex twice from CH_3CN by addition of diethyl ether. Characterization of Cu-fubmpa was done by elemental analysis, X-ray crystallography, and UV-vis spectroscopy. The single crystals for X-ray crystallography were obtained via liquid-liquid diffusion in an NMR tube, with Cu-fubmpa dissolved in chloroform and layered with diethyl ether. A projection of the, structure is shown in Figure 5.1. In the crystal structure, the top axial OTf^- ligand has a

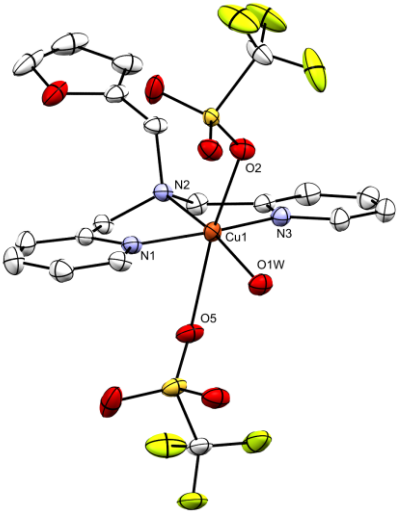

Figure 5.1. Crystal structure of Cu-fubmpa as determined by X-ray crystallography. All hydrogen atoms are omitted for clarity.

Cu–O bond distance of 2.375(1) Å. However, the Cu1–O5 distance between the copper centre and the second triflate is 2.665(2) Å. This is on the long side for an axial Cu–O bond, and points to a more square pyramidal coordination environment rather than an octahedral geometry.[22-25] Both elemental analysis and X-ray crystallography show that a water molecule is coordinated to the copper centre, likely originating from the $Cu(OTf)_2$ salt, which has a tendency to form hydrates when exposed to air. The coordinated water molecule forms a hydrogen bond (1.980 Å) with one of the oxygen atoms of the axial triflate ligand below the plane. Additionally, the crystal structure confirms that the furanyl group does not coordinate to the Cu centre. UV-vis spectra were measured in MilliQ water, and the extinction coefficient (ε) for the d-d transition at 660 nm is 1.0×10^2 L mol^{-1} cm^{-1}, and for the absorption peak at 251 nm an ε of 9.7×10^3 L mol^{-1} cm^{-1} was found (Appendix D.1).

5.2.2. Electrochemistry of Cu-fubmpa, Cu-bpmpa, and Cu-pmea

To study the effect of the different ligands on the redox chemistry of the complexes, cyclic voltammograms of the complexes in a pH 7 phosphate buffer (PB) solution under argon atmosphere were recorded using a Glassy Carbon (GC) working electrode (A = 0.0707 cm^2). The resulting redox couples recorded of Cu-fubmpa, Cu-bpmpa, and Cu-pmea with a scan rate of 100 mV s^{-1} are combined in Figure 5.2, with Cu-tmpa as the reference complex. The $E_{1/2}$ of the $Cu^{II/I}$ redox couples of these complexes span a wide potential range (Table 5.1), shifting positively from the $E_{1/2}$ of 0.21 V for Cu-tmpa to 0.25 V for Cu-fubmpa, 0.37 V Cu-pmea, and 0.49 V for Cu-bpmpa. All three complexes

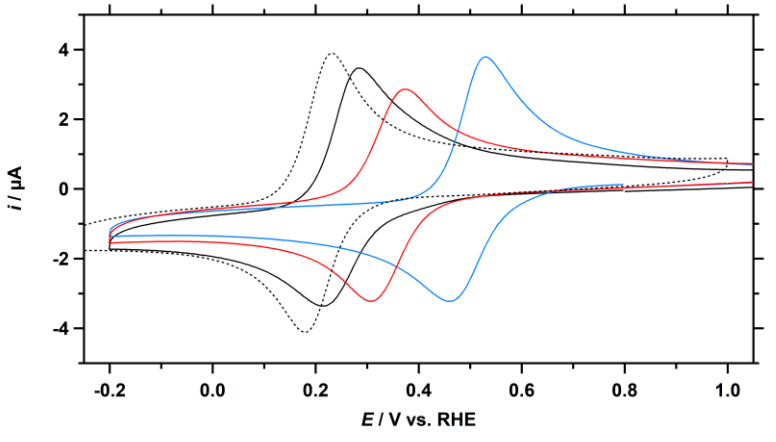

Figure 5.2. Cyclic voltammograms of Cu-fubmpa (black), Cu-pmea (red), and Cu-bpmpa (blue), including Cu-tmpa (dotted) as a reference, in a pH 7 phosphate buffer under 1 atm Ar. For each copper complex a concentration of 0.3 mM was used. Conditions: pH 7 PB ($[PO_4]$ = 100 mM), 293 K, 100 mV s^{-1} scan rate, 0.0707 cm^2 electrode surface area.

Table 5.1. Overview of the redox potentials ($E_{1/2}$), the peak-to-peak separation (ΔE_p) between the peak oxidation and peak reduction potentials, and the diffusion coefficients of the different investigated copper complexes.

Complex	$E_{1/2}$ (V vs. RHE) [a]	ΔE_p (mV) [a]	D (cm^2 s^{-1}) [b]
Cu-tmpa [c]	0.206	56	4.9×10^{-6}
Cu-fubmpa	0.248(2)	73	2.4×10^{-6}
Cu-pmea	0.341(2)	68	2.9×10^{-6}
Cu-bpmpa	0.494(2)	71	2.3×10^{-6}

[a] *Determined from CV measured at 100 mV s^{-1}.* [b] *Determined from i_{pc}.* [c] *Data from Chapter 2.*

show lower peak redox currents (i_p) than Cu-tmpa for both the cathodic (i_{pc}) and anodic (i_{pa}) peaks.

To determine the diffusion coefficient (D) for these complexes, CVs were measured at different scan rates, varying from 10 to 500 mV s^{-1}, for each complex and are shown in Figure D.2. In the same figure, the corresponding Randles-Sevcik plots show that good linearity ($R^2 > 0.99$) is achieved for the i_{pc} and i_{pa} as a function of the square root of the scan rate. This indicates that the complexes behave as diffusive homogenous species near the electrode under inert conditions, and potential deposition of the complex on the electrode surface does not play a significant role. By applying the Randles-Sevcik equation (Eq. 5.1), the diffusion coefficients of the Cu^{II} species were determined from the i_{pc} values, which resulted in diffusion coefficients of 1.3×10^{-6} cm^2 s^{-1} for Cu-fubmpa, 2.3×10^{-6} cm^2 s^{-1} for Cu-bpmpa, and 2.9×10^{-6} cm^2 s^{-1} for Cu-pmea, which are lower than that of Cu-tmpa (4.9×10^{-6} cm^2 s^{-1}).[8]

$$i_p = 0.446nFSC_{cat}^0\sqrt{\frac{F\nu}{RT}D_{cat}} \tag{5.1}$$

The redox couples of all the complexes seem to be fully reversible, but analysis of the peak-to-peak separation (ΔE_p) shows a small deviation from the ideal 59 mV peak-to-peak separation for a fully reversible system, averaging a ΔE_p increase of 10 mV at a 100 mV s^{-1} scan rate. To investigate whether this is the case over a larger range of scan rates, Laviron plots of the oxidative (E_{pa}) and reductive peak (E_{pc}) potentials were constructed (Figure D.3). An increase of the ΔE_p with increasing scan rate is observed for all three complexes, especially at scan rates above 100 mV s^{-1}. This increase is largely caused by a shift of the E_{pa} of the respective complexes towards higher potentials, while the E_{pc} remain stable or show much smaller shifts. As a result, the $E_{1/2}$, which is defined as the midway potential between the E_{pc} and E_{pa}, is also affected. For Cu-fubmpa and Cu-bpmpa, this leads to an apparent positive shift of the $E_{1/2}$ at scan rates above 100 mV s^{-1} (Figured D.4). Cu-pmea sees both the E_{pa} and E_{pc} equally shift towards higher

and lower potentials, respectively, leading to a stable $E_{1/2}$ as a function of scan rate. The increase in peak-to-peak separation resulting from a shifting E_{pa} may point to slower electron transfer rate for the oxidation of the Cu^{I} species,[26] although the effect is marginal with only an increase of 15–20 mV observed for the ΔE_p.

5.2.3. Electrocatalytic performance towards the ORR and HPRR

We have previously shown that Cu-tmpa produces H_2O_2 as a detectable intermediate during the electrocatalytic reduction of O_2,[8] but it can also further reduce H_2O_2 to H_2O (Chapters 2 and 3). Therefore, both the oxygen reduction reaction (ORR) and the hydrogen peroxide reduction reaction (HPRR) were studied for Cu-fubmpa, Cu-bpmpa, and Cu-pmea. CVs were measured in a pH 7 phosphate buffer solution containing 0.3 mM of the complex under 1 atm O_2 or with 1.1 mM H_2O_2 under 1 atm Ar. The resulting catalytic waves for the reduction of O_2 and H_2O_2 are shown in Figure 5.3 separately for each catalyst. One observation that can immediately be made is that the ORR current is greater than the HPRR current for all the analysed complexes, which was also observed for Cu-tmpa. For Cu-fubmpa, the onset of the ORR appears to be ca. 40 mV

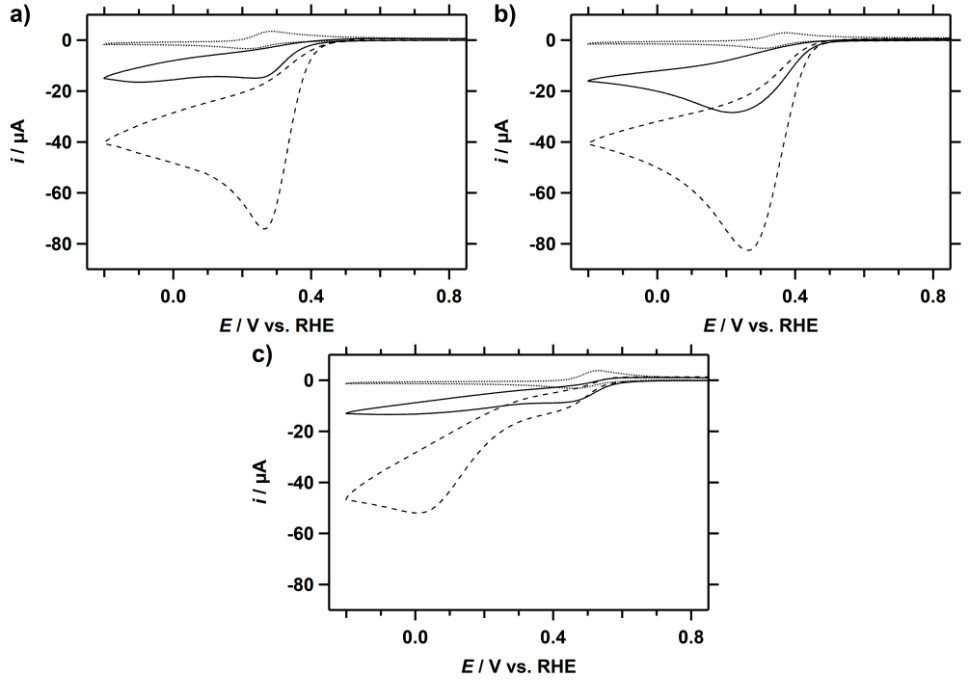

Figure 5.3. CVs of Cu-fubmpa **(a)**, Cu-pmea **(b)**, and Cu-bpmpa **(c)** in a PB pH 7 electrolyte solution under 1 atm Ar (dotted line), 1 atm O_2 (dashed line), or with 1.1 mM H_2O_2 under 1 atm Ar (solid line). For each catalyst, a concentration of 0.3 mM was used. Conditions: pH 7 PB ($[PO_4]$ = 100 mM), 293 K, 100 mV s^{-1} scan rate, 0.0707 cm^2 electrode surface area.

lower compared to the onset of the HPRR (Figure D.5). On the other hand, both Cu-bpmpa and Cu-pmea each show overlapping catalytic onsets for the ORR and HPRR. The HPRR onset for Cu-fubmpa is shifted to a lower potential, something that was also observed for Cu-tmpa (Chapter 3).

The catalytic linear sweep voltammograms (LSV) of complexes Cu-fubmpa, Cu-bpmpa, and Cu-pmea of the ORR and HPRR have been combined in Figure 5.4 to allow for a straightforward comparison between the catalysts. The catalytic wave of the ORR in the presence of Cu-fubmpa overlaps neatly with the catalytic wave of Cu-tmpa, while the catalytic onset potential of Cu-pmea is slightly higher. However, both catalysts reach somewhat lower peak catalytic current i_{cat} than Cu-tmpa, indicating a lower catalytic rate, while taking into account that O_2 diffusion limitations come into play at 1 atm O_2 for Cu-tmpa. Cu-bpmpa on the other hand shows a much earlier onset than the other catalysts, nearer to the 0.695 V vs. RHE equilibrium potential of the O_2/H_2O_2 couple. However, a trade-off for this higher onset potential is the much lower catalytic activity exhibited by the catalyst. Additionally, a second, larger catalytic wave is observed at a much lower potential. The half-wave potential of the first catalytic wave of Cu-bpmpa is the same as the equilibrium potential of the redox couple in the absence of O_2. This equivalence, where $E_{1/2}$ is equal to $E_{cat/2}$, is expected for a system that is not limited in substrate. This behaviour is not observed for the $E_{cat/2}$ of Cu-fubmpa (+90 mV) or Cu-pmea (+25 mV) at catalyst concentration of 0.3 mM. However, for Cu-bpmpa no limiting current plateau is maintained and the catalytic current increases again at potentials below 0.3 V vs. RHE. In this potential window, the background current generated by the glassy carbon electrode needs to be accounted for, as GC readily reduces O_2 to H_2O_2 below 0.3 V. This could be the main contributing factor to the catalytic current observed in the lower potential region. Background correction on the

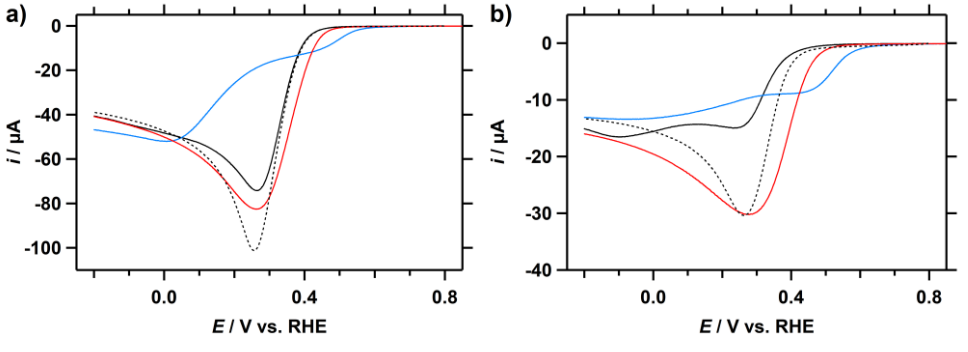

Figure 5.4. Linear sweep voltammograms (LSV) of Cu-fubmpa (black), Cu pmea (red), and Cu- bpmpa (blue), including Cu-tmpa (dotted) as a reference, under 1 atm O_2 **(a)**, or in the presence of 1.1 mM H_2O_2 under 1 atm Ar **(b)**. For each catalyst, a concentration of 0.3 mM was used. Conditions: pH 7 PB ($[PO_4]$ = 100 mM), 293 K, 100 mV s^{-1} scan rate, 0.0707 cm^2 electrode surface area.

Table 5.2. Catalytic parameters for the ORR by Cu-fubmpa, Cu-pmea, and Cu-bpmpa, in a pH 7 phosphate buffer under 1 atm O_2 (1.2 mM).

Complex	$E_{onset,\ ORR}$	$E_{cat/2}$	$E_{cat,\ ORR}$	i_{cat} (μA)
Cu-tmpa [c]	0.50	0.31	0.23	−90
Cu-fubmpa	0.49	0.34	0.26	−62
Cu-pmea	0.50	0.37	0.26	−79
Cu-bpmpa	0.61	0.50 [a]	0.40 [a]	−24 [a]
		0.19 [b]	0.10 [b]	−12 [b]

[a] values for the first catalytic wave. [b] values for the second catalytic wave. [c] Data from Chapter 2. Potentials are reported vs. RHE. Conditions: pH 7 PB ([PO_4] = 100 mM), 0.3 mM catalyst concentration, 293 K, 100 mV s^{-1} scan rate, 0.0707 cm^2 electrode surface area.

catalytic waves was performed (Figure D.6), which shows that the second catalytic wave is much less prominent than in Figure 5.4, but is still present and reaches a peak catalytic current i_{cat} at 0.1 V vs. RHE. An overview of the catalytic parameters for the ORR by all three complexes is shown in Table 5.2.

The voltammetry data from the HPRR show a similar trend for the onset potential of the catalytic reaction, with the onset in presence of Cu-fubmpa < Cu-pmea < Cu-bpmpa (Figure 5.4bb). Of the three catalysts investigated here, the highest catalytic rates are observed for Cu-pmea, reaching an i_{cat} of −30 μA, which is the same maximum current as observed for Cu-tmpa. However, the slope of the catalytic wave is somewhat less steep than that of Cu-tmpa, while the peak-width is larger. A lower slope, and thus a smaller increase in catalytic rate as a function of applied potential, hints at a lower HPRR rate constant for Cu-pmea. The catalytic current of Cu-fubmpa is significantly lower, with an i_{cat} of −15 μA, and seemingly reaches a plateau, although the $E_{cat/2}$ is still roughly 80 mV higher than the $E_{1/2}$ of the catalyst. It is therefore unclear whether this points to a S-shaped catalytic curve where substrate diffusion is no longer the limiting factor, or whether another process is inhibiting catalytic activity as the applied potential

Table 5.3. Catalytic parameters for the HPRR by Cu-fubmpa, Cu-pmea, and Cu-bpmpa, in a pH 7 phosphate buffer in the presence of 1.1 mM H_2O_2 under 1 atm Ar.

Complex	$E_{onset,\ HPRR}$	$E_{cat/2}$	$E_{red,\ HPRR}$	i_{cat} (μA)
Cu-tmpa [a]	0.45	0.34	0.26	−30
Cu-fubmpa	0.45	0.33	0.23	−15
Cu-pmea	0.52	0.36	0.28	−30
Cu-bpmpa	0.61	0.52	0.40	−11

[a] Data from Chapter 3. Potentials are reported vs. RHE. Conditions: pH 7 PB ([PO_4] = 100 mM), 0.3 mM catalyst concentration, 293 K, 100 mV s^{-1} scan rate, 0.0707 cm^2 electrode surface area.

is reduced. A small second peak is observed at potentials below 0 V vs. RHE. Curiously, a second broad catalytic wave is once again visible for Cu-bpmpa during the HPPR, similar to what was observed for the ORR. The catalytic parameters for the HPRR are summarized in Table 5.3.

5.2.4. Determination of catalytic rate constants for the ORR and HPRR using the foot-of-the-wave analysis

While comparing voltammograms of different complexes under catalytic conditions can already hint at the relative catalytic performance of these catalysts, it will not give the entire picture. This is especially true when the catalytic conditions are such that substrate limitations occur, as can easily be the case during the ORR which is limited to an O_2 concentration of roughly 1.2 mM at room temperature (293 K) under atmospheric pressure. In the case of Cu-tmpa this was shown to be a limiting factor for the catalytic reaction. Thus, limitations in substrate diffusion may result in similar peak catalytic currents for catalysts with significant variation in catalytic rate constants. Two different approaches can be taken to elucidate the catalytic rate constants for a given catalyst; by determining the current enhancement under non-limiting conditions, which in practice means lowering the catalyst concentration; alternatively, the foot-of-the-wave analysis (FOWA) method can be used. The FOWA extrapolates the ideal or maximum turnover frequency (TOF_{max}) of the catalyst from the foot of the catalytic wave, close to the onset of the catalytic reaction (see Appendix A for a detailed description). While a very powerful tool, care must be taken in choosing the parameters with which to perform the calculations. The catalytic electron number n_{cat} is one such parameter, and the reduction of O_2 can either lead to H_2O_2 (n_{cat} = 2) or H_2O (n_{cat} = 4) as the product. In the previous section, Cu-bpmpa and Cu-pmea were shown to each have the same onset for the ORR and HPRR, therefore a n_{cat} of 4 is appropriate for these complexes. Conversely, Cu-fubmpa has a 40 mV lower onset potential for the HPRR than for the ORR. By comparing the CVs of the ORR and HPRR in the foot of the wave potential window, it was determined that the charge transferred during the HPPR is less than 10% of the total charge for ORR in the region where the potential windows overlap. This makes a n_{cat} of 2 more appropriate when determining the TOF_{max} of Cu-fubmpa for the ORR, as the contribution of hydrogen peroxide reduction is minimal. For the FOWA, CVs were measured in triplicate in a PB (pH 7) electrolyte solution containing 0.3 mM complex and 1 atm O_2 (for the ORR), or 1.1 mM H_2O_2 in the presence of 1 atm Ar (for the HPRR), using a freshly polished GC electrode for each measurement. These voltammograms were used to construct plots of the current enhancement i_c/i_p vs $\left(1 + exp\left[\mathrm{F}/RT\left(E - E_{1/2}\right)\right]\right)^{-1}$, where i_c is the catalytic current measured in the presence of catalyst and substrate (O_2 or H_2O_2) at the applied potential E. In the foot-of-the-wave

Table 5.4. TOF_{max} for the ORR and HPRR derived from the foot-of-the-wave analysis (FOWA).

Complex	**TOF_{max} (s^{-1})**	
	ORR	*HPRR*
Cu-tmpa [c]	$1.8\times10^{6} \pm 0.6\times10^{6}$ [a]	$2.1\times10^{5} \pm 0.1\times10^{5}$
Cu-fubmpa	$1.3\times10^{5} \pm 0.3\times10^{5}$ [a]	$0.8\times10^{3} \pm 0.1\times10^{3}$
Cu-pmea	$3.7\times10^{2} \pm 0.6\times10^{2}$ [b]	$1.0\times10^{3} \pm 0.3\times10^{3}$
Cu-bpmpa	0.7 ± 0.1 [b]	6.4 ± 0.9

[a] $n_{cat} = 2$. [b] $n_{cat} = 4$. [c] *Data from Chapters 2 and 3. Conditions: 0.3 mM catalyst concentration, pH 7 PB ([PO_4] = 100 mM), 293 K, 100 mV s^{-1} scan rate, 0.0707 cm^2 electrode surface area.*

potential window, a linear fit was obtained between the catalytic onset and the potential where i_c/i_p is at least equal to 1.6. The onset is defined as $i_c/i_{redox} \geq 2$, where i_{redox} is the current measured at the applied potential E in the presence of the catalyst, but without any substrate present in solution. The TOF_{max} was determined from the slope of the linear fit, by applying Eq. 5.2.

$$\frac{i_c}{i_p} = \frac{2.24 n_{cat}\sqrt{\frac{RT}{Fv}TOF_{max}}}{1 + exp\left[\frac{F}{RT}\left(E - E_{1/2}\right)\right]} \tag{5.2}$$

The resulting TOF_{max} for the ORR and HPRR are reported in Table 5.4. For the ORR, Cu-fubmpa has the highest TOF_{max}, while Cu-bpmpa has the lowest (0.7 s^{-1}). For the HPRR, Cu-pmea shows the highest TOF_{max}, but is closely followed by Cu-fubmpa. All catalyst discussed here have a lower TOF_{max} than Cu-tmpa for both catalytic reactions. Comparison of the ORR and HPRR TOF_{max} reveals an interesting trend. The relative magnitude of the TOF_{max} of both catalytic reactions changes with increasing $E_{1/2}$ of the complexes. For Cu-fubmpa, the ORR is much faster than the HPRR, while for Cu-bpmpa, which has the highest $E_{1/2}$, the ORR is slower than the HPRR. For Cu-pmea, both reactions show similar TOF_{max}. Thus, the higher the $E_{1/2}$, and thus the catalytic onset potential, the more the reduction of H_2O_2 seems to be favoured over the reduction of O_2. However, the FOWA does not consider the second, higher catalytic wave observed for Cu-bpmpa in the presence of O_2, as the TOF_{max} is derived from the initial slope around 0.6 V vs. RHE. This second catalytic wave, which is centred at 0.1 V vs. RHE, cannot be accurately probed by the FOWA but shows that higher catalytic rates can be achieved by Cu-bpmpa (or a different catalytic species, see discussion below) at the cost of a significantly increased overpotential.

5.2.5. Comparison between FOWA and catalytic current enhancement at low catalyst concentrations

Another method to determine the catalytic performance is by direct determination using the catalytic current enhancement derived from the i_{pc} of the catalyst and the i_{cat}.[27] Ideally, this should be done under more reliable kinetic conditions, such that substrate diffusion is not the main limiting factor during the catalytic reaction. In the case of a highly active ORR catalyst, this requires measurement of the current enhancement at low catalyst concentration. However, the determination of the i_{pc} at low catalyst concentration is complicated by the relatively much larger double layer current of the electrode. Therefore, the i_{pc} is derived from the Randles-Sevcik equation (Eq. 5.1), using the calculated diffusion coefficient of the catalyst and the catalyst concentration. The i_{cat} values were obtained from background-corrected LSVs measured at several catalyst concentrations in the range of 1 to 30 µM, depending on the catalyst, under 1 atm O_2 (see Appendix D.7). The k_{obs} were derived from the current enhancement (i_{cat}/i_p) using Eq. 5.3, in the concentration range where a linear dependency of the i_{cat} on the catalyst concentration was observed. Eq 5.3 and Eq 5.2 are equal for the case when the applied potential E is lower than the $E_{1/2}$, as the $\left(1 + exp\left[\mathrm{F}/RT\left(E - E_{1/2}\right)\right]\right)^{-1}$ term goes to unity, and a maximum catalytic current is reached, where $i_c = i_{cat}$.

$$\frac{i_{cat}}{i_{pc}} = 2.24n\sqrt{\frac{RT}{Fv}k_{obs}} \tag{5.3}$$

This resulted in ORR k_{obs} of $2.0\times10^3 \pm 0.6\times10^3$ s^{-1} for Cu-fubmpa, $2.0\times10^4 \pm 0.2\times10^4$ s^{-1} for Cu-pmea, and $0.7\times10^3 \pm 0.1\times10^3$ s^{-1} for Cu-bpmpa (Figure 5.5a), all of which are lower than the k_{obs} of Cu-tmpa (2.0×10^5) which was determined using the same method.[8] Comparing the k_{obs} to the previously determined TOF_{max}, a large difference of three orders of magnitude is observed for the rate constants of Cu-bpmpa. As mentioned in the last section, the TOF_{max} of this complex describes the catalytic rate constant associated with the first catalytic wave, while the k_{obs} was determined from the peak catalytic current around 0.13 V at low catalyst concentration (Figure D.7e), which corresponds to the second catalytic wave observed. A catalytic current associated with the first catalytic wave cannot be observed at these low catalyst concentrations (Figure D.7e).

If Eq 5.3 is applied to the smaller first catalytic wave in the presence of 0.3 mM Cu-bpmpa and 1 atm O_2 (Figure D.4), a k_{obs} of 0.6 s^{-1} is obtained. Here, the catalytic peak current of the first catalytic wave (E_{cat} = 0.4 V vs. RHE) was used as i_{cat}, while i_{pc} was obtained from the redox couple of the complex under inert atmosphere. This k_{obs}

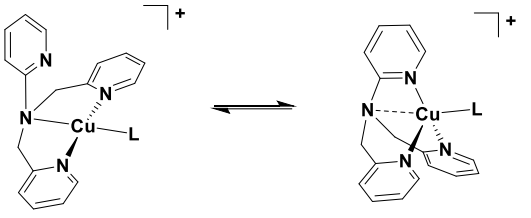

Scheme 5.3. Proposed conversion to a more tetrahedral coordination geometry of the Cu^{I}-bpmpa complex.

value (0.6 s^{-1}) corresponds closely to the FOWA-derived TOF_{max} of the ORR (0.7 s^{-1}) under the same catalytic conditions (0.3 mM Cu-bpmpa, 1 atm O_2).

The cause of the two distinct catalytic waves during the ORR at 0.4 and 0.1 V vs. RHE is unclear. It is not the result of different onsets of the (partial) ORR and the HPRR, which could result in H_2O_2 only being reduced at a lower potential, as these catalytic reactions have the same onsets (see Table 5.2 and 5.3). Moreover, the HPRR is an order of magnitude faster than the ORR at the first catalytic wave. One possibility for the increased ORR activity at a lower potential is a change in the coordination geometry of the Cu^{I} complex. Crystal structures of $[Cu^{II}(bpmpa)(Cl)(ClO_4)]$ and $[Cu^{II}(bpmpa)Cl_2]$ complexes show a (distorted) square-pyramidal coordination environment, with bpmpa coordinating through the two pyridyl nitrogen atoms and the tertiary amine nitrogen as a tridentate ligand.[12] This is a similar coordination geometry as observed for Cu^{II}-bmpa (bmpa = bis(2-pyridylmethyl)amine).[28] In contrast, Cu^{I} complexes favour a tetrahedral geometry, which is difficult to attain due to the tridentate nature of the bpmpa ligand.[29] For Cu^{I}-tmpa it has been shown that the Cu–N_{amine} bond can be elongated, facilitating a more tetrahedral-like geometry.[30] While no crystal structures for Cu^{I} complexes of Cu-bpmpa have been reported thus far, elongation of the Cu–N_{amine} bond followed by coordination of the previously uncoordinated pyridine to the Cu centre may result in a more tetrahedral coordination environment (Scheme 5.3). As the pyridine donor in the aminopyridine moiety has a more electron-donating character than the tertiary amine, this would result in more electron density on the Cu^{I} centre, which would coincide with a lower equilibrium potential. This proposed reorganization of the ligand in the coordination environment may be assisted by the coordination of dioxygen and formation of the Cu^{II}–$OO^{\bullet-}$ complex, which would facilitate the elongation of the Cu–N_{amine} bond.

The k_{obs} of Cu-pmea was found to be slightly less than two orders of magnitude higher than the TOF_{max}. In general, for the same catalytic reaction and catalytic species, the k_{obs} obtained from the peak catalytic current is lower than the ideal TOF_{max}. While substrate depletion has been reduced by increasing the ratio between O_2 and the

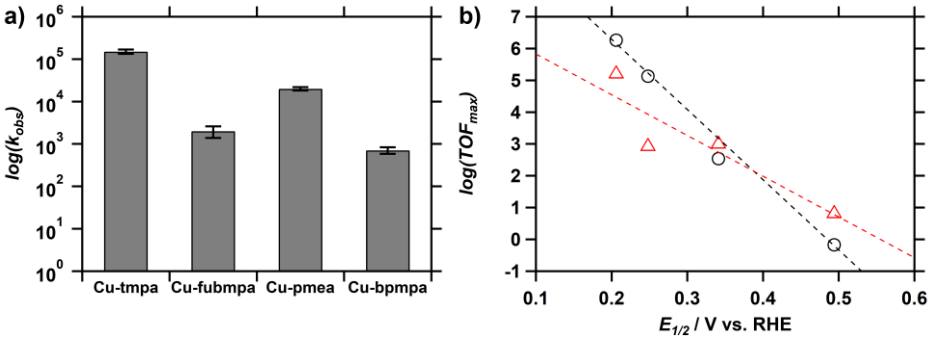

Figure 5.5. a) Plot of the ORR k_{obs} of Cu-fubmpa, Cu-pmea, and Cu-bpmpa derived from the current enhancement (i_c/i_p) at low catalyst concentration. **b)** Plot of the logarithm of the TOF_{max} of the ORR (circles; 1 atm O_2) and HPRR (triangles; 1.1 mM H_2O_2) versus the $E_{1/2}$ of the respective catalysts, including Cu-tmpa ($E_{1/2}$ = 0.21 V).

catalyst under the conditions where the k_{obs} for Cu-pmea was determined, other processes may still negatively affect the catalytic reaction and thus decrease the measured k_{obs}. This holds true for the other two catalysts described here, including Cu-tmpa.[8] The contradictory results for Cu-pmea can also not be explained by a potential erroneous choice of n_{cat} in the previous section, as even if a n_{cat} of 2 is used for the FOWA, it would still result in a lower TOF_{max} than the k_{obs}. Additionally, at low catalyst concentration the half-wave potential $E_{cat/2}$ during ORR is equal to the $E_{1/2}$ of the catalyst, confirming that the species present under non-catalytic conditions is also responsible for the peak current under catalytic conditions and thus for the measured k_{obs}. While no overlapping catalytic peaks are observed during differential pulse voltammetry measurements under catalytic conditions (Figure D.8), it is possible that an equilibrium between two different Cu-pmea complexes is present. One candidate would be the copper complex wherein one of the pyridine arms is not coordinated, which would have a redox potential closer to that of Cu-fubmpa. This species may be in an unfavourable equilibrium with the fully (tetradentate) coordinated copper complex, resulting in different catalytic rate constants being observed in the two different potential windows.

Variation in the length of the $(-CH_2)_n$ spacer (where n = 0–2) between the central tertiary amine and one of the pyridine moieties results in a significant shift in the equilibrium potential of the Cu^{II}/Cu^{I} redox couple. The shifts of Cu-pmea and Cu-bpmpa towards a higher potential are much larger than observed for Cu-fubmpa, in which one of the pyridine arms is replaced for a furanyl group, thereby keeping the central tertiary amine intact while preventing coordination of a third ligand arm to the Cu centre. In this way the effect of a lower denticity on the catalytic activity could be investigated without removing the pyridine arm entirely, which would introduce a secondary amine

that could be easily oxidized during the catalytic cycle. Indeed, the $E_{1/2}$ of Cu-fubmpa and Cu-bmpa (bmpa = bis(2-pyridylmethyl)amine) are nearly identical in a pH 7 phosphate buffer,[21] indicating that coordination of the furanyl group does not occur while in solution.

A linear relationship between the maximum TOF [log(TOF_{max})] and the $E_{1/2}$ of the catalytic species is observed, as visualized in Figure 5.5b. As the catalyst $E_{1/2}$ increases, and thus the overpotential decreases, the rate of the reaction decreases. This behaviour seems to hold for both the ORR and the HPRR, although a lower slope is apparent for the decline in HPRR TOF_{max}. The slopes associated with these linear relationships are 44 mV per decade for the ORR, and 65 mV per decade for the HPRR. Similar behaviour has been observed for proton reduction by molecular nickel catalysts, where a linear relationship was observed between the log(TOF) and the driving force for H_2 elimination, $\Delta G°_{H2}$, which is directly dependent on the $E_{1/2}$ of the $Ni^{II/I}$ redox couple and the pK_a of the pendant amine in the second coordination sphere.[31] This scaling of the TOF_{max} with the overpotential is a well-known phenomenon for molecular electrocatalysts, and has been shown for a range of nickel, cobalt and iron complexes capable of catalysing the ORR or hydrogen evolution reaction (HER).[31-35] Thus far, this scaling relationship has only been circumvented by designing a catalyst of which the $E_{1/2}$ is sensitive to pK_a changes and the nature of the acid–conjugate base mixture.[36] We were able to reduce the overpotential of the ORR by almost 300 mV by changing the spacer length of one the pyridine arms. This resulted in an overpotential of less than 200 mV for the 2-electron ORR (E^0 = 0.695 V vs. RHE) catalysed by Cu-bpmpa. However, the copper catalysts are still subject to the scaling relations, limiting the catalytic rates at the lower overpotentials. Interestingly, Figure 5.5b also shows that at a certain potential the relative activities for the ORR and HPRR invert, and the HPRR becomes the faster catalytic reaction of the two reactions as the $E_{1/2}$ of the catalyst is increased. This indicates that the reduction of H_2O_2 is less affected by the thermodynamic and kinetic limitations that govern the scaling relations, as the rate at which the HPRR TOF_{max} decreases with increasing $E_{1/2}$ (or with the reduction of the overpotential) is less than observed for the ORR.

5.3. Conclusion

The influence of structural changes of the tetradentate tmpa-based ligand scaffold on the electrochemical reduction of O_2 and H_2O_2 has been investigated. The changes of the coordination geometry around the Cu centre, induced by varying the length of the $(\text{-}CH_2)_n$ spacer of one of the pyridine arms, resulted in significant positive shifts of the thermodynamic $Cu^{II/I}$ redox potentials of up to 300 mV for Cu-bpmpa (n = 0). The magnitude of the potential shift seems to be the related to the strain that is placed on

the preferred coordination environment of the Cu^{II} or Cu^{I} centres. The increase in redox potentials relative to Cu-tmpa resulted in a corresponding increase of the catalytic onset potentials, which for the ORR was confirmed under conditions where substrate limitations were minimized, for which a clear increase of the catalytic half-wave potential was observed. Thus, the overpotential for the ORR and HPRR directly relate to the redox potential of the copper catalyst. Additionally, a clear linear scaling relationship was observed between the $\log(TOF_{max})$ for the ORR and the $E_{1/2}$ of the catalyst. The maximum TOF decreases as the onset potential increases, highlighting the well-established trade-off between kinetics and thermodynamics which has been observed for many electrochemical reactions, both for heterogenous catalysts and homogenous molecular catalysts. However, to the best of our knowledge this is the first time that this has been demonstrated for the 2-electron reduction of O_2 to H_2O_2 by a molecular copper catalyst. The same relationship was observed for the reduction of H_2O_2, although a smaller decrease of TOF_{max} was observed with increasing redox potential. This also resulted in higher rate constants for the HPRR than the ORR in the case of Cu-bpmpa, which is contrary to the catalytic behaviour observed for the other copper complexes. This eliminates H_2O_2 as significant a by-product of the ORR by Cu-bpmpa, over the entire catalytic potential window.

Thus, we were able to significantly reduce the overpotential related to the ORR by modifying the primary coordination sphere of the copper complexes, and have shown that this results in a linear relationship, and a trade-off, between the catalytic rate and the overpotential for these copper-based electrocatalysts.

5.4. Experimental

5.4.1. General

All precursors used in the ligand synthesis were obtained from Sigma-Aldrich/Merck. $Cu(OTf)_2$ was obtained from Alfa Aesar. All other chemicals and solvents were purchased from commercial suppliers. Whatman® RC60 membrane filters were used for the filtration and isolation of the synthesized copper complexes. NMR spectra were recorded on a Bruker 400 MHz or Bruker DPX 300 spectrometer. ESI MS mass spectra were obtained on a Thermo Fisher Scientific MSQ Plus. UV-vis spectra were recorded on a Varian Cary® 40 UV-vis spectrophotometer, or a HORIBA Aqualog spectrophotometer. Elemental analysis was performed by Mikroanalytisches Laboratorium Kolbe. Aqueous electrolyte solutions were prepared using NaH_2PO_4 (Suprapur®, Merck) and Na_2HPO_4 (Suprapur®, Merck). Milli-Q Ultrapure grade water was used in all electrochemical experiments and for the preparation of all aqueous electrolyte solutions. H_2O_2 was obtained from Sigma-Aldrich (≥30%, for ultratrace analysis), and the exact concentration was determined via permanganate titration. pH

measurements were performed on a Hanna Instruments HI 4222 pH meter which was calibrated by five-point calibration using IUPAC standard buffers. Alumina suspensions (1.0, 0.3, and 0.05 µm) for electrode polishing were obtained from Buehler. All gasses used during electrochemical measurements, H_2, O_2, and argon (each 5.0 grade), were supplied by Linde.

5.4.2. Synthesis

5.4.2.1. *N-(Furan-2-ylmethyl)-N-[bis(2-pyridyl)methyl]amine (fubmpa)*

2-pyridine carboxaldehyde (0.38 mL, 4 mmol) and furan-2-ylmethanamine (0.18 mL, 2 mmol) were added to dry 1,2-dichloroethane (10 mL) and stirred for 1 hour. Sodium triacetoxyborohydride (1.272 g, 6 mmol) was added and the mixture was stirred for 24 hours at room temperature under N_2 atmosphere. $NaHCO_3$ (sat.aq.; 10 mL) was added to the mixture and stirred for one hour to quench the reaction. The organic layer was then separated, concentrated and the residue was purified over alumina column eluting with EtOAc/PetEt/MeOH = 50:50:0.5. After removal of the solvent by rotary evaporation at reduced pressure, the product was obtained as a pale, yellow oil (0.388 g, 1.39 mmol, 69% yield). ESI MS m/z (found (calc)): 280.0 (280.1, $[M + H^+]^+$). ^{1}H NMR (400 MHz, $CDCl_3$) δ 8.52 (ddd, *J* = 4.9, 1.8, 1.0 Hz, 2H, py-*H*6), 7.65 (ddd, *J* = 7.8, 7.4, 1.8 Hz, 2H, py-*H*4), 7.58 (ddd, *J* = 7.8, 1.2, 1.0 Hz, 2H, py-*H*3), 7.38 (d, *J* = 1.8 Hz, 1H, fu-*H*5), 7.13 (ddd, *J* = 7.4, 4.9, 1.2 Hz, 2H, py-*H*5), 6.30 (dd, *J* = 3.2, 1.8 Hz, 1H, fu-*H*4), 6.23 (d, *J* = 3.2 Hz, 1H, fu-*H*3), 3.85 (s, 4H, py-CH_2), 3.74 (s, 2H, fu-CH_2). ^{13}C NMR (101 MHz, $CDCl_3$) δ 159.5 (py-*C*2), 152.1 (fu-*C*2), 149.0 (py-*C*6), 142.1 (fu-*C*5), 136.5 (py-*C*4), 122.9 (py-*C*3), 122.0 (py-*C*5), 110.1 (fu-*C*4), 109.0 (fu-*C*3), 59.7 (py-*C*H_2), 50.4 (fu-*C*H_2).

5.4.2.2. *N-[bis(2-pyridyl)methyl]-2-pyridylamine (bpmpa)*

A modified literature procedure was used for the synthesis of bpmpa. Sodium hydride (60% in mineral oil; 720 mg, 18 mmol) was added to anhydrous DMF (15 mL) under N_2. 2-aminopyridine (286 mg, 3 mmol) was dissolved in anhydrous DMF (15 mL) under N_2 and subsequently added to the sodium hydride solution and stirred for 30 minutes. 2-chloromethylpyridine•HCl (984 mg, 6 mmol) in anhydrous DMF (20 mL) was added dropwise to the solution over a period of 30 minutes under N_2. The solution was heated to 50 °C and stirred for 24 hours. The resulting black solution was carefully quenched with water (50 mL) which resulted in a yellow solution. A saturated $NaHCO_3$ solution (50 mL) was added, followed by extraction with DCM (4 × 120 mL). The combined organic fractions were subsequently washed with more saturated $NaHCO_3$ solution (3 × 50 mL). The solvent was evaporated by rotary evaporation under reduced pressure and the resulting dried crude product was further purified by silica column chromatography. The crude was dissolved in a few millilitres of DCM, loaded on silica,

and the product was obtained with a 98:2 DCM/MeOH mixture as eluent. The product fractions were combined, and the solvent removed by rotary evaporation under reduced pressure. The product was obtained as a slightly yellow oil (441 mg, 1.6 mmol, 53% yield). ^{1}H NMR (400 MHz, $CDCl_3$) δ 8.53 (dd, *J* = 5.0, 1.9, 2H), 8.17 (ddd, *J* = 5.0, 2.0, 1.0 Hz, 1H), 7.58 (td, *J* = 7.7, 1.9 Hz, 2H), 7.37 (ddd, *J* = 8.6, 7.2, 1.9 Hz, 1H), 7.22 (d, *J* = 7.7 Hz, 2H), 7.13 (dd, *J* = 7.7, 5.0, 2H), 6.59 (7.2, 5.0, 1H), 6.47 (dd, *J* = 8.6, 1.0 Hz, 1H), 4.96 (s, 4H).

5.4.2.3. *bis[(2-pyridyl)methyl]-2-(2-pyridyl)ethylamine (pmea)*

Pyridine-2-carboxyaldehyde (2.25 g, 21 mmol, 2 equiv.) was added to a stirred mixture of 2-(2-pyridyl)ethylamine (1.28 g, 10.5 mmol, 1 equiv.) and sodium triacetoxyborohydride (6.21 g, 21 mmol, 1 equiv.) in dry EDC (100 mL). Molecular sieves were added to remove H_2O during the reaction. This mixture was stirred under argon for seven days. Subsequently, $NaHCO_3$ (sat.aq.; 100 mL) was added and the mixture was stirred for 30 minutes. The mixture was filtered to remove molecular sieves. The crude mixture was then washed with $NaHCO_3$ (sat.aq) (2x 50 mL) and the organic phase was dried with $MgSO_4$ and filtered again. The EDC was evaporated at 40 °C by rotary evaporation. The crude was dissolved in DCM and extracted with an aqueous solution of pH 4 (acidified with HCl; 3 × 30 mL). The pH of the combined aqueous solution was increased to pH 9 by addition of saturated $NaHCO_3$ and extracted with DCM (6 × 50 mL). The combined organic layers were dried with Na_2SO_4 followed by filtration. The solvent was removed by rotary evaporation at reduced pressure. TLC (Aluminium oxide; 100:10 EtOAc/MeOH) revealed the presence of some impurities close to the baseline. The crude was dissolved in a few millilitres of DCM, loaded on Aluminium oxide, and the product (R_f = 0.7) was obtained using a 100:10 EtOAc/MeOH mixture as eluent. The product fractions were combined, and the solvent removed by rotary evaporation under reduced pressure. The resulting brown oil was exhaustively extracted with warm pentane. Evaporation of the pentane resulted in a colourless oil (1.92 g, 6.3 mmol, 60% yield). ESI MS m/z (found (calc)): 305.2 (305.2, $[M + H^+]^+$), 327.1 (327.2, $[M + Na^+]^+$). ^{1}H NMR (300 MHz, $CDCl_3$) δ 8.53 – 8.42 (m, 3H), 7.54 (qd, J = 7.5, 1.8 Hz, 3H), 7.33 (dt, *J* = 7.8, 1.1 Hz, 2H), 7.09 (m, 4H), 3.87 (s, 4H, C*H*$_2$), 3.08 – 2.89 (m, 4H, C*H*$_2$-C*H*$_2$).

5.4.2.4. *Synthesis of [Cu(fubmpa)(H_2O)($OTf)_2$]*

Fubmpa (0.2 g, 0.716 mmol) and $Cu(OTf)_2$ (0.259 g, 0.716 mmol) were dissolved in CH_3CN (10 mL) and together stirred for 1 hour. Following this, the solvent was removed by rotary evaporation at reduced pressure and the complex was dissolved in a minimal amount of CH_3CN until fully dissolved. Diethyl ether was slowly added until the solution became clouded, upon which a few drops of CH_3CN were added to make sure the complex was fully dissolved, and the solution remain homogenous. The solution was

put in the freezer at −18 °C for the crystals to form. This crystallization was done twice to make sure the complex was pure. After filtration of mixture, the complex; [**1**](OTf)$_2$ was obtained as a navy blue solid (0.315 g, 0.479 mmol, 67%). ESI MS m/z (found (calc)): 211.9 (212.0 [M - OH_2 - 2OTf + 2MeCN]$^{2+}$), 387.0 (387.1 [M - OH_2 - 2OTf + $HCOO^-$]$^+$). Elemental analysis calcd (%) for $C_{19}H_{19}CuF_6N_3O_8S_2$: C 34.63, H 2.91, N 6.38; found: C 34.27, H 3.04, N 6.66. UV-Vis: λ_{max} (ε in L mol^{-1} cm^{-1}) in milliQ water = 251 nm (9740); 660 nm (99).

5.4.2.5. *Synthesis of [Cu(bpmpa)(CH_3CN)](OTf)$_2$*

Cu(OTf)$_2$ (1.5 mmol, 542 mg) was dissolved in dry CH_3CN (5 mL) under N_2 atmosphere. and bpmpa (1.5 mmol, 419 mg) in dry CH_3CN (30 mL) was subsequently added to the solution. A dark green solution formed immediately, and the solution was stirred for 1 hour. The solvent was removed by rotary evaporation under reduced pressure and the dark green solid was dissolved in a minimal amount of CH_3CN until fully dissolved. Diethyl ether was added until the solution became clouded, after which a few drops of CH_3CN were added to make sure the complex was fully dissolved. The solution was put in the freezer at −18 °C for 3 days, allowing for crystallization of the complex. The dark turquoise crystals were filtered off and washed with Et_2O. Yield: 72% (1.08 mmol, 730 mg). ESI MS m/z (found (calc)): 210.6 (210.5 [M - 2OTf + 2MeCN]$^{2+}$), 384.0 (384.1 [M - 2OTf + $HCOO^-$]$^+$). Elemental analysis calcd (%) for $C_{21}H_{19}CuF_6N_5O_6S_2$ + 0.6 H_2O: C 36.56, H 2.95, N 10.15; found: C 36.50, H 2.83, N 10.08.

5.4.2.6. *Synthesis of [Cu(pmea)(CH_3CN)](OTf)$_2$*

Cu(OTf)$_2$ (3 mmol, 913 mg) was dissolved in dry CH_3CN (5 mL) under N_2 atmosphere. and bpmpa (3 mmol, 1085 mg) in dry CH_3CN (30 mL) was subsequently added to the solution. A dark turquoise solution formed immediately, and the solution was stirred for 1 hour. The solvent was removed by rotary evaporation under reduced pressure. The crude complex was dissolved in minimal amounts of $CHCl_3$ until fully dissolved. Methyl tert-butyl ether (MTBE) was added until the solution became clouded, after which a few drops of $CHCl_3$ were added to make sure the complex was fully dissolved. The solution was put in the freezer at −18 °C for 7 days, allowing for crystallization of the complex. The solution separated into a dark blue crystalline solid and a small amount of a green oil-like substance. The supernatant, including the green oil, were decanted from the round-bottom flask, and the remaining blue crystalline solid was washed with a 30:70 $CHCl_3$/MTBE (50 mL) and filtered off. The solid was crushed into smaller pieces and dried under vacuum. Yield: 82% (2.46 mmol, 1.74 g). ESI MS m/z (found (calc)): 204.2 (204.0 [M - 2OTf]$^{2+}$), 412.1 (412.1 [M - MeCN- 2OTf + $HCOO^-$]$^+$), 516.0 (516.1 [M – MeCN - OTf]$^+$). Elemental analysis calcd (%) for $C_{23}H_{23}CuF_6N_5O_6S_2$ + 0.3 $CHCl_3$: C 37.67, H 3.16, N 9.43; found: C 37.78, H 3.22, N 9.41.

5.4.3. Electrochemical measurements

All electrochemical experiments were performed using a custom-built 10 mL single-compartment glass cell with a three-electrode setup. The measurements were performed using Autolab PGSTAT 12, 204, and 128N potentiostats, operated by the Autolab NOVA 2 software. The working electrode is a PEEK encapsulated GC disk (A = 0.071 cm^2, Metrohm) submerged in the solution. Unless otherwise stated, the GC electrode was manually polished before each catalytic measurement for 5 mins with 1.0, 0.3, and 0.05 µm alumina suspensions on Buehler cloth polishing pads, or with a Struers LaboPol-30 polishing machine using 1.0 µm diamond and 0.04 µm silica suspension on polishing cloths (Dur-type) for 1 min each. This was followed by sonication of the electrode in Milli-Q purified water for 10–15 minutes. A gold wire was used as a counter electrode and was flame annealed and rinsed with Milli-Q purified water. The reference electrode was a reversible hydrogen electrode (RHE) made from a Pt mesh submerged in same electrolyte solution as the main cell compartment, connected via a Luggin capillary, and the reference compartment was continuously saturated with H_2 gas. Oxygen-free electrolyte solutions were prepared by saturating the cell for 20 to 30 minutes with Ar, after which an atmosphere of 1 atm Ar was maintained over the solution. Oxygen-saturated electrolyte solutions were obtained by saturating the cell for 20 minutes with O_2, after which a 1 atm O_2 atmosphere was maintained over the solution.

Prior to each experiment, the glassware was fully submerged and boiled in MilliQ purified water. Additionally, all glassware was regularly cleaned by submersion in an aqueous oxidizing solution containing 0.5 M H_2SO_4 and 1 mg/mL (6.3 mM) $KMnO_4$ overnight. This is followed by removal of excess $KMnO_4$ and MnO_2 from the glassware with diluted H_2SO_4 and H_2O_2, followed by rinsing the glassware three times with water and boiling twice submerged in Milli-Q purified water.

5.5. References

[1] H. A. Gasteiger, S. S. Kocha, B. Sompalli, F. T. Wagner, *Appl. Catal. B* **2005**, *56*, 9-35.
[2] O. Gröger, H. A. Gasteiger, J.-P. Suchsland, *J. Electrochem. Soc.* **2015**, *162*, A2605-A2622.
[3] Z. P. Cano, D. Banham, S. Ye, A. Hintennach, J. Lu, M. Fowler, Z. Chen, *Nat. Energy* **2018**, *3*, 279-289.
[4] S. Fukuzumi, Y. Yamada, K. D. Karlin, *Electrochim. Acta* **2012**, *82*, 493-511.
[5] L. An, T. S. Zhao, X. L. Zhou, L. Wei, X. H. Yan, *RSC Adv.* **2014**, *4*, 65031-65034.
[6] S. H. Zeronian, M. K. Inglesby, *Cellulose* **1995**, *2*, 265-272.
[7] G. Grigoropoulou, J. H. Clark, J. A. Elings, *Green Chem.* **2003**, *5*, 1-7.
[8] M. Langerman, D. G. H. Hetterscheid, *Angew. Chem. Int. Ed.* **2019**, *58*, 12974-12978.
[9] K. D. Karlin, J. C. Hayes, S. Juen, J. P. Hutchinson, J. Zubieta, *Inorg. Chem.* **1982**, *21*, 4106-4108.
[10] E. A. Ambundo, M.-V. Deydier, A. J. Grall, N. Aguera-Vega, L. T. Dressel, T. H. Cooper, M. J. Heeg, L. A. Ochrymowycz, D. B. Rorabacher, *Inorg. Chem.* **1999**, *38*, 4233-4242.
[11] M. Schatz, et al., *Inorg. Chem.* **2001**, *40*, 2312-2322.
[12] Simon P. Foxon, O. Walter, S. Schindler, *Eur. J. Inorg. Chem.* **2002**, *2002*, 111-121.

[13] T. Fujii, A. Naito, S. Yamaguchi, A. Wada, Y. Funahashi, K. Jitsukawa, S. Nagatomo, T. Kitagawa, H. Masuda, *Chem. Commun.* **2003**, 2700-2701.
[14] D. Das, Y.-M. Lee, K. Ohkubo, W. Nam, K. D. Karlin, S. Fukuzumi, *J. Am. Chem. Soc.* **2013**, *135*, 2825-2834.
[15] G. S. Patterson, R. H. Holm, *Bioinorganic Chemistry* **1975**, *4*, 257-275.
[16] A. W. Addison, *Inorg. Chim. Acta* **1989**, *162*, 217-220.
[17] H. Nagao, N. Komeda, M. Mukaida, M. Suzuki, K. Tanaka, *Inorg. Chem.* **1996**, *35*, 6809-6815.
[18] H. R. Lucas, G. J. Meyer, K. D. Karlin, *J. Am. Chem. Soc.* **2010**, *132*, 12927-12940.
[19] Y. Lee, et al., *Inorg. Chem.* **2009**, *48*, 11297-11309.
[20] S. Kakuda, R. L. Peterson, K. Ohkubo, K. D. Karlin, S. Fukuzumi, *J. Am. Chem. Soc.* **2013**, *135*, 6513-6522.
[21] N. W. G. Smits, B. van Dijk, I. de Bruin, S. L. T. Groeneveld, M. A. Siegler, D. G. H. Hetterscheid, *Inorg. Chem.* **2020**, *59*, 16398-16409.
[22] B. J. Hathaway, P. G. Hodgson, *J. Inorg. Nucl. Chem.* **1973**, *35*, 4071-4081.
[23] K. J. de Almeida, N. A. Murugan, Z. Rinkevicius, H. W. Hugosson, O. Vahtras, H. Ågren, A. Cesar, *Phys. Chem. Chem. Phys.* **2009**, *11*, 508-519.
[24] R. F. See, R. A. Kruse, W. M. Strub, *Inorg. Chem.* **1998**, *37*, 5369-5375.
[25] A. Nimmermark, L. Öhrström, J. Reedijk, **2013**, *228*, 311-317.
[26] R. S. Nicholson, I. Shain, *Anal. Chem.* **1964**, *36*, 706-723.
[27] R. M. Bullock, A. M. Appel, M. L. Helm, *Chem. Commun.* **2014**, *50*, 3125-3143.
[28] N. Niklas, F. W. Heinemann, F. Hampel, T. Clark, R. Alsfasser, *Inorg. Chem.* **2004**, *43*, 4663-4673.
[29] M. Palaniandavar, R. J. Butcher, A. W. Addison, *Inorg. Chem.* **1996**, *35*, 467-471.
[30] B. S. Lim, R. H. Holm, *Inorg. Chem.* **1998**, *37*, 4898-4908.
[31] W. J. Shaw, M. L. Helm, D. L. DuBois, *BBA - Bioenergetics* **2013**, *1827*, 1123-1139.
[32] M. L. Pegis, B. A. McKeown, N. Kumar, K. Lang, D. J. Wasylenko, X. P. Zhang, S. Raugei, J. M. Mayer, *ACS Cent. Sci.* **2016**, *2*, 850-856.
[33] Y.-H. Wang, M. L. Pegis, J. M. Mayer, S. S. Stahl, *J. Am. Chem. Soc.* **2017**, *139*, 16458-16461.
[34] M. L. Pegis, C. F. Wise, B. Koronkiewicz, J. M. Mayer, *J. Am. Chem. Soc.* **2017**, *139*, 11000-11003.
[35] C. M. Klug, A. J. P. Cardenas, R. M. Bullock, M. O'Hagan, E. S. Wiedner, *ACS Catal.* **2018**, *8*, 3286-3296.
[36] D. J. Martin, B. Q. Mercado, J. M. Mayer, *Sci. Adv.* **2020**, *6*, eaaz3318.